



UNIVERSITY OF LEEDS

This is a repository copy of *Resolving the location of small intercontinental earthquakes using Open Access seismic and geodetic data: lessons from the 18 January 2017 mb 4.3 Ténéré, Niger, earthquake.*

White Rose Research Online URL for this paper:
<https://eprints.whiterose.ac.uk/185634/>

Version: Accepted Version

Article:

Craig, T orcid.org/0000-0003-2198-9172 and Gibbons, S (Accepted: 2022) Resolving the location of small intercontinental earthquakes using Open Access seismic and geodetic data: lessons from the 18 January 2017 mb 4.3 Ténéré, Niger, earthquake. *Geophysical Journal International*. ISSN 0956-540X (In Press)

This item is protected by copyright, This article has been accepted for publication in *Geophysical Journal International*. Published by Oxford University Press on behalf of the Royal Astronomical Society.

Reuse

Items deposited in White Rose Research Online are protected by copyright, with all rights reserved unless indicated otherwise. They may be downloaded and/or printed for private study, or other acts as permitted by national copyright laws. The publisher or other rights holders may allow further reproduction and re-use of the full text version. This is indicated by the licence information on the White Rose Research Online record for the item.

Takedown

If you consider content in White Rose Research Online to be in breach of UK law, please notify us by emailing eprints@whiterose.ac.uk including the URL of the record and the reason for the withdrawal request.



eprints@whiterose.ac.uk
<https://eprints.whiterose.ac.uk/>

Resolving the location of small intracontinental earthquakes using Open Access seismic and geodetic data: lessons from the 18 January 2017 m_b 4.3, Niger, earthquake

Timothy J. Craig

COMET, School of Earth and Environment, The University of Leeds,
Leeds, United Kingdom. LS2 9JT

t.j.craig@leeds.ac.uk

Steven J. Gibbons

NGI, Sognsveien 72, N-0855 Oslo, Norway

March 25, 2022

Abstract

A low-magnitude earthquake was recorded on January 18, 2017, in the Ténéré desert in northern Niger. This intraplate region is exceptionally sparsely covered with seismic stations and the closest open seismic station, G.TAM in Algeria at a distance of approximately 600 km, was unusually and unfortunately not operational at the time of the event. Body-wave magnitude estimates range from m_b 4.2 to m_b 4.7 and both seismic location and magnitude constraints are dominated by stations at teleseismic distances. The seismic constraints are strengthened considerably by array stations of the International Monitoring System for verifying compliance with the Comprehensive Nuclear Test-Ban-Treaty. This event, with magnitude relevant to low-yield nuclear tests, provides a valuable validation of the detection and location procedure for small land-based seismic disturbances at significant distances. For seismologists not in the CTBT system, the event is problematic as data from many of the key stations are not openly available. We examine the uncertainty in published routinely-determined epicenters by performing multiple Bayesloc location estimates with published arrival times considering both all published arrival times and those from open stations only. This location exercise confirms lateral

uncertainties in seismologically-derived location no smaller than 10 km. Coherence for InSAR in this region is exceptionally high, and allows us to confidently detect a displacement of the order 6 mm in the time-frame containing the earthquake, consistent with the seismic location estimates, and with a lateral length scale consistent with an earthquake of this size, allowing location constraint to within one rupture length (≤ 5 km) – significantly reducing the lateral uncertainty compared with relying on seismological data only. Combining Open Access-only seismological and geodetic data, we precisely constrain the source location, and conclude that this earthquake likely had a shallow source. We then discuss potential ways to continue the integration of geodetic data in the calibration of seismological earthquake location.

Keywords: Earthquake source observations, Seismicity and tectonics, Satellite geodesy, Earthquake hazards, Earthquake monitoring and test-ban treaty verification

1 Introduction

On the 18th January, 2017, a small-magnitude earthquake occurred in the Ténéré desert of northern Niger (Figure 1a). Located at the northern edge of the Sahel, bordering the Sahara, and roughly half way between the coasts of West Africa and the Red Sea, the source region is deep in the interior of Africa, far from any major population centres – the nearest city being Agadez, ~ 400 km away. The region is similarly remote from a tectonic perspective - the nearest active plate boundaries are in northern Morocco (~ 2000 km), the Gulf of Suez (~ 2400 km) and the East Africa Rift System (≥ 3000 km). The nearest instrumentally-recorded earthquake to the 2017 event, of any magnitude, in the combined catalogues of Bulletin of the International Seismological Centre (ISC Bulletin hereafter; ISC (2021)), is a similarly-remote $m_b 4.5$ earthquake in the southern Ahaggar mountains of Algeria, ~ 600 km away. Within 15 degrees (~ 1650 km) of the Ténéré earthquake, there are only 625 earthquakes reported in the full ISC Bulletin, of any magnitude.

As a result of the tectonic quiescence and remoteness of the region, Ténéré is one of the least-well seismologically instrumented continental regions on Earth, with the nearest seismic station located over 600 km away (at Tamanrasset, southern Algeria - which was in fact inoperative at the time of this earthquake), and no other stations within 1000 km. For small-magnitude earthquakes, data from seismic networks at local and regional distances is crucial for the robust and accurate determination of the earthquake location (e.g. Bondár et al, 2004). In the absence of such data, the 2017 Ténéré earthquake offers an opportunity to test the resolving power of global seismic networks, and the limitations of seismological location routines in the absence of near-field data. With the lack of vegetation, and the lack of major agricultural or industrial activity in the area, the Ténéré desert is also a region where the coherence of interferometric synthetic aperture

25 radar (InSAR) images is high, enabling the detection of small-magnitude surface displace-
26 ments, and we thus also aim to test how satellite geodesy can complement seismological
27 approaches in the location of small earthquakes in remote continental areas.

28 Routine seismological catalogues determined the location ($\sim 19.6^\circ N, 10.6^\circ E$), and
29 magnitude ($m_b 4.2 - 4.7$) of this earthquake (see Table 1). The reported magnitude of
30 this earthquake places it in the range of interest for low-yield nuclear tests (e.g. Barker
31 et al, 1998; Chun et al, 2011). For such events, routine seismological monitoring is supple-
32 mented by the observational capabilities of the International Monitoring System (IMS),
33 under the auspices of the Comprehensive Test Ban Treaty Organisation (CTBTO), most
34 particularly through a global network of small-aperture seismic arrays and high-quality
35 three-component seismometers. However, data from many of these networks remain
36 subject to access restrictions, and are not currently freely available to the scientific com-
37 munity. This study probes how far events like the Ténéré earthquake can be studied
38 and characterised in detail using only freely-available Open Access data, and tests how
39 reliant the location of such earthquakes is on closed-access data. We combine remote
40 seismological and geodetic analysis to assess the validity with which routine processing
41 approaches were able to determine the location of this earthquake. We highlight a num-
42 ber of issues that may cause problems for the location of rare small earthquakes in remote
43 continental interiors, and demonstrate how the combination of careful seismological anal-
44 ysis with modern geodetic data can mitigate such problems, allowing the high-resolution
45 characterisation of such events.

46 2 Overview of the Seismological Observations

47 Figure 1 displays the source region of the January 18, 2017, earthquake together with
48 the locations of events in the ISC GEM catalog (ISC-GEM, 2021) (unrestricted) and
49 the ISC Bulletin (limited to those within 15°), and the locations of seismic stations
50 used to constrain the location in the bulletins listed in Table 1. The map in panel (a)
51 confirms both the absence of significant seismic events in an almost continental-scale
52 region surrounding the epicenter and the sparsity of stations at local, regional, or far-
53 regional distances contributing to the location estimates. Of those stations at far-regional
54 distances (a term usually referring to distances between 10° and 20°) only the three-
55 component station GT.DBIC in the Ivory Coast is open for public access. Panels (b),
56 (c) and (d) of Figure 1 show the signal on GT.DBIC both in a high frequency bandpass
57 (1-4 Hz) and the lower frequency band from 12.5 s to 50.0 s period. The short-period
58 band signals are typical of far-regional continental propagation with high frequency Pn
59 and Sn arrivals followed by high-amplitude and slightly lower period Lg waves which
60 dominate the wavetrain. Both Pn and Sn arrivals are followed by long codas with high-
61 frequency energy. Both body waves and surface waves are visible in the longer period

62 signal although the Pn and Sn arrivals have low Signal-to-Noise Ratio (SNR). Only
63 the Pn arrival is particularly useful for location purposes; the Sn arrival is extremely
64 emergent and picking an accurate signal onset is difficult. In addition, even if the Pn
65 arrival-time can be read accurately, the distance-range for this station is associated with
66 an exceptionally large uncertainty in the modelled traveltime (e.g. Myers et al, 2015). The
67 primary value of the DBIC signal is in the estimation of magnitude and the hypothesis
68 that the event is relatively shallow in order to explain the dominant Lg and surface waves.

69 Figure 2 provides both a representative selection of the available teleseismic waveforms
70 and an overview of the global station coverage, again differentiating between stations open
71 to the general public and those limited to authorized parties in the CTBT system. For
72 a seismic event with significant continental landmass in all directions within distances of
73 100 degrees (i.e. where you would anticipate observing P -waves) there is an exceptional
74 degree of asymmetry to the observing seismic network. We have examined significant
75 numbers of open waveforms at stations not included in the ISC bulletin, but where
76 data is openly available (see Figure 1a), and found in very few cases signals which both
77 offered a high SNR and a useful location, covering an azimuthal or distance gap relative
78 to the network displayed in Figure 2. The best signals are found on stations to the
79 North East; in Eastern Europe and Central Asia – a distribution that will be the result
80 of both the network coverage, and the orientation of the focal mechanism and resultant
81 radiation pattern (note that the focal mechanism for this earthquake is unknown). Figure
82 2 shows signals on the vertical components of three 3-component stations, and (vertical
83 component) array beams on three array stations.

84 Of the waveforms shown on Figure 2, the Makanchi array (MKAR) is a 9-site primary
85 IMS seismic array in Kazakhstan, the Mount Meron array (MMAI) is a 16-site auxiliary
86 IMS seismic array in Israel, and the Bukovina array (BURAR) is a non-IMS 9-element
87 array in Romania. The data from all of these arrays are openly available; MKAR and
88 BURAR are available via the IRIS Data Management Center and MMAI is available via
89 the GEOFON data center at GFZ Potsdam. Each of these arrays has an aperture of
90 only a few km, with the intention that short period signals (e.g. 1-4 Hz) are coherent
91 between sensors and that the SNR of signal arrivals can be improved by delay-and-
92 stack beamforming (e.g. Rost and Thomas, 2009). Similarly, estimating the coherence
93 or relative power of beams in different directions allows us to estimate the backazimuth
94 and apparent velocity of incoming wavefronts. This assists in algorithms to associate
95 detections and helps to build confidence that a given signal detection is indeed associated
96 with our event hypothesis, on the basis of directional coherence of arrivals.

97 For each array in Figure 2, the top panel shows the array beam constructed using
98 the predicted backazimuth and P -wave slowness, based on the ISC location. Beneath
99 each of the array beams is a scan of backazimuth as a function of time (for a fixed
100 apparent velocity based on the expected earthquake epicentre) and a scan of apparent

101 velocity as a function of time (for a fixed value of the backazimuth based on the expected
102 earthquake epicentre). These plots are a variant on the VESPA process (Davies et al,
103 1971) and allow us to confirm that each of the signals at the time of the predicted P -
104 arrival is associated with a coherent wave packet with a direction consistent with the
105 origin hypothesis. Gibbons et al (2016) performed such analysis on several array stations
106 for an earthquake of similar magnitude near the Northern tip of Novaya Zemlya in the
107 Russian Arctic and found double bursts of coherent energy with a delay of just over 3
108 seconds at stations at different azimuths from the epicenter. This observation supported
109 a hypothesis of teleseismic pP phases which helped to constrain the event depth. There
110 is no such unambiguous evidence of depth phases in the array analysis in Figure 2.
111 BURAR and MMAI show very little coherent energy in the coda following the initial
112 arrival; MKAR shows coherent energy with appropriate propagation parameters far into
113 the coda.

114 The remaining three panels of Figure 2 show signals for the P -arrivals at arbitrarily
115 chosen teleseismic 3-component stations (in Czechia, Saudi Arabia, and Kenya). We note
116 that the SNR for the signals at many of these stations is relatively poor, and that im-
117 provement through stack-and-delay is not possible for non-array stations. The waveforms
118 shown in Figure 2 also highlight the potential subjectivity in identifying the onset of a
119 particular phase arrival, with the majority of arrivals being emergent, especially in terms
120 of identifying a confirmed signal above the level of noise. We see no unmistakable depth
121 phases, which would offer a high-precision constraint on the event depth. A few stations
122 show multiple bursts of energy but there is insufficient evidence at any station to label
123 with confidence the later arrivals as depth phases.

124 Summarising the available seismological data, we are left with a comparatively sparse
125 set of phase observations, of variable, but often limited, precision. The advantages in
126 signal identification and arrival precision that arise from the enhanced processing of
127 small aperture arrays is clear. But only a few of the operators of these stations make
128 their waveform data Open Access (see Figure 2). Similarly, many of the more isolated
129 three-component stations, vital for filling gaps in azimuthal and epicentral coverage,
130 remain closed to the general public. Combined, these pose the question of how reliant
131 high-precision earthquake location is on closed-access data, and how well characterised
132 events such as the Ténéré earthquake can be, using only Open Access seismic data.

133 **3 Seismic Location Estimates for the 18 January** 134 **2017 Niger Earthquake**

135 Figure 3 shows the epicenters listed in Table 1 together with their published 95% con-
136 fidence ellipses. The epicenters reported by the NEIC/USGS (National Earthquake In-

137 formation Center/United States Geological Survey) and CTBTO/IDC (Comprehensive
138 Nuclear Test-Ban-Treaty Organization/International Data Center) lie comfortably within
139 the confidence ellipse reported by the other agency, and there is significant overlap be-
140 tween the two confidence ellipses. The epicenter reported by the International Seismolog-
141 ical Center (ISC, 2021) lies within both of these confidence ellipses but is itself associated
142 with a much smaller confidence ellipse which does include the CTBT epicenter estimate,
143 but not the NEIC epicenter estimate. A fourth location estimate is provided in the ISC
144 catalog summary: the ISC-EHB estimate (ISC-EHB, 2021), named after Engdahl, van
145 der Hilst, and Buland. This epicenter lies to the southeast and outside of all of the other
146 95% confidence ellipses. The ISC-EHB estimate itself is associated with a far smaller con-
147 fidence ellipse which overlaps little with the other 95% confidence ellipses. All of these
148 confidence ellipses share a similar azimuth of the semi-major axis: all around 120° . This
149 is easy to understand in terms of the station distribution (c.f. Figure 2) since the density
150 of contributing stations in directions from North to East (i.e. in Europe and Central
151 Asia) is substantially greater than in other directions. The final location estimate is that
152 from the European Mediterranean Seismological Center (EMSC, e.g. Godey et al, 2013)
153 and this lies approximately 20 km to the South East of the ISC and CTBT locations.
154 Like the NEIC estimate, the EMSC solution is published fairly rapidly and is attributed
155 a relatively large confidence ellipse. However, the EMSC solution is more dominated
156 by stations to the North (Europe) than the NEIC solution which is consistent with the
157 rather different epicenter estimate and orientation of the confidence ellipse. Given the
158 discrepancy between the EMSC solution and the ISC and CTBT locations, we will not
159 be subjecting the EMSC solution to further analysis.

160 Comparing the various epicenters and corresponding confidence ellipses is difficult
161 since the solutions use varying combinations of arrival-time readings, station distributions,
162 weights, and location algorithms. Only the NEIC, CTBT, and EMSC catalogs are truly
163 independent. Although the solutions have a number of stations in common, the readings
164 are made by different analysts and using different systems and location procedures. The
165 ISC catalog, and the ISC-EHB solution, exploit phase readings from multiple catalogs and
166 can frequently use two or more alternative arrival time estimates, reported by different
167 agencies, for the same phase arrival to constrain an event. TORD in southwestern Niger
168 and KEST in Tunisia are two of the stations in the ISC bulletin that are closest to the
169 earthquake epicenter (see Figure 1). Both stations are primary seismic stations of the
170 International Monitoring System and, to the best of our knowledge, the data from neither
171 are available to users other than those with access authorized by National Data Centers
172 in the CTBT system. The USGS has access to this data via the United States National
173 Data Center and is authorized to use arrival-time estimates from these stations when
174 forming their earthquake bulletin.

175 The ISC bulletin provides two estimates for the P_n arrival time at TORD: 21:50:53.534

176 and 21:51:02.71, reported by the IDC and the NEIC respectively. Only the first of these
177 is a defining phase in the ISC catalog, with a time residual of -0.7 seconds. The second
178 is labelled a “Questionable onset” (with a time residual of 8.5 seconds) and does not
179 contribute to the solution. The ISC bulletin also provides two estimates for the P_n
180 arrival time at KEST: 21:52:07.30 and 21:52:06.98, again provided by the IDC and the
181 NEIC respectively. Both of these arrivals (with time-residuals of -0.7 seconds and -1.0
182 seconds respectively) are defining arrivals in the ISC solution. In the ISC-EHB bulletin,
183 all four of these arrival times are defining phases for the location estimates with time
184 residuals listed as -2.1 seconds (TORD P_n , IDC), 7.1 seconds (TORD P_n , NEIC), -1.4
185 seconds (KEST P_n , IDC), and -1.7 seconds (KEST P_n , NEIC). The time residual on the
186 TORD P_n arrival is large for both the ISC and ISC-EHB solutions. The size of the time
187 residual led it to be disregarded from the ISC solution. While it is a defining phase in
188 the ISC-EHB solution, it is not easy to estimate the effect it has on the solution without
189 a thorough examination of the weights and the provenance of the location algorithm.

190 The discrepancy between the ISC-EHB epicenter and the other epicenters is likely
191 a combination of many such differences. The waveforms displayed in Figures 1 and 2
192 make it clear how emergent and ambiguous some of the phase arrival time estimates
193 may be. Often the highest amplitude comes several seconds after what appears to be
194 the first signal onset and we may have to make judgements regarding what is a likely
195 first P -arrival and what is a possible depth phase. The first part of the signal visible
196 above the background noise may be significantly later than the true onset time if we have
197 an emergent signal or a depth phase with a higher amplitude than the first P -arrival.
198 Without access to the waveform data, it is not possible for an independent seismologist to
199 evaluate the quality of the arrival time estimates, limiting our ability to determine where
200 pick uncertainty may be driving the discrepancies in location estimates. The seismic
201 event location procedures employed at the different agencies are under continual revision
202 and overviews of recent progress at the NEIC and IDC are given by Benz (2017) and Koch
203 (2013) respectively. Details of improvements to the ISC location algorithm can be found
204 in Bondár and Storchak (2011) and references therein. A comprehensive description of
205 the exact procedures employed at a given observatory, so detailed that they could be
206 reproduced exactly by a different observatory, is unrealistic.

207 However, we can gain more understanding as to how the location estimates depend
208 upon the choice of stations alone by performing new location estimates using a common
209 algorithm with the arrival times used for the different catalogs displayed in Figure 3.
210 We use the Bayesloc program (Myers et al, 2007) which can solve for the locations of
211 multiple seismic events simultaneously by a Monte Carlo Markov Chain (MCMC) pro-
212 cedure to find a joint probability distribution for the events’ origins, origin parameter
213 uncertainties, and for empirical corrections to modelled traveltimes. Prior constraints,
214 for example Ground Truth event locations or existing models for traveltime corrections,

215 can be applied if available to improve the quality of the posterior probability distribu-
216 tions. Although the program is designed for, and is most effective with, large clusters of
217 seismicity, it can also be run for a single event. Having only a single event of course pre-
218 cludes, for example, the calculation of empirical traveltimes corrections (since we cannot
219 resolve between the contributions to arrival-time anomalies resulting from velocity varia-
220 tions and those resulting from picking errors). For each iteration of the MCMC routine,
221 the program writes out the epicenter coordinates. Over a single run, many thousands of
222 origin hypotheses are written out generating a cloud. The size and shape of this cloud
223 provides a visualization of the uncertainty associated with the location which may show
224 a more complex geometry than the classical formal confidence ellipses. Given the absence
225 of prior constraints, and the fact that we only have a single event, our main motivation
226 for using Bayesloc is this ability to visualize any irregularities in the geometry of the
227 location probability distribution.

228 Figure 4 displays the clouds of trial epicenter estimates from the Bayesloc calculations
229 for four different combinations of stations. In panel (a) the event is located using only the
230 phase arrival times listed in the USGS/NEIC bulletin. The red symbols are the epicenters
231 output when we only use those stations for which waveform data can be obtained without
232 barrier by an arbitrary user from only open sources (red symbols in panel (b)). The grey
233 symbols are the epicenters output when we also allow use of the arrival times from stations
234 for which waveform data are not available without specific authorization (white symbols
235 in panel (b)). We attempt to better visualize the spread of the point clouds by plotting
236 the 90, 95, and 99% confidence ellipses based upon the statistics of the coordinates,
237 although we stress that the point cloud distributions may display significant departures
238 from the geometries indicated by the ellipses. The inclusion of the closed access stations
239 reduces the apparent spread somewhat although the difference is not large. As noted
240 earlier, the TORD arrival in this dataset is associated with a large time-residual and so
241 it may have had very little influence on the solutions. We note also that the Bayesloc
242 epicenter clouds using the USGS/NEIC arrival estimates are consistent with the bulletin
243 epicenter estimate.

244 Panel (c) of Figure 4 shows the corresponding Bayesloc epicenter clouds for the ar-
245 rivals listed in the ISC bulletin, with the corresponding station maps displayed in panel
246 (d). There is a significant difference between the spread of the epicenter clouds for the
247 “complete” and “strictly open” station networks for the ISC arrivals. We note that not
248 only is the TORD time-residual far smaller for one of the arrivals in the ISC solution,
249 but there are 3 other network stations, KIC, TIC, and LIC which add extra constraints
250 from the South West. These stations are all very close to DBIC, in the Ivory Coast, and
251 they do not much increase the azimuthal coverage. However, their inclusion may change
252 the weight of the constraints from that direction considerably. We note in addition, an
253 extra constraint from the Sonca Array (ESDC) in Spain from the CTBT bulletin. This

254 is in a direction in which there are no open stations with good signals or clear picks. This
255 may be an example of where the use of beamforming of signals on a seismic array may
256 make a usable phase arrival where one was not sufficiently strong on a single channel,
257 allowing the identification of arrivals even in regions where the radiation pattern leads
258 to comparatively low amplitudes. The Bayesloc epicenter clouds lie a few km to the
259 South East of the ISC bulletin epicenter, and to the West of the epicenter provided in
260 the ISC-EHB bulletin. The differences in the location estimates are likely due to both
261 different weightings of the phase arrivals and differences in the location algorithms.

262 To summarize, with the available seismic stations, there is a lateral uncertainty of
263 at least 10 km in the epicentral estimates. The epicenter from the ISC-EHB bulletin
264 appears to be an outlier and, given the set of arrivals from which this solution is formed,
265 the quoted 95% confidence interval would appear to be optimistic. We can move the
266 epicenter estimate by several km by changing the observing network alone, but never by
267 more than around 10 km. Had the seismic signals from this event had characteristics of
268 an explosion, the confidence region from the seismic signals is sufficient for the criteria
269 for a permissible On-Site-Inspection following Entry Into Force of the Comprehensive
270 Nuclear Test-Ban-Treaty. The treaty text states “The area of an on-site inspection shall
271 be continuous and its size shall not exceed 1,000 square kilometres. There shall be no
272 linear distance greater than 50 kilometres in any direction” (UN, 1998). Even with the
273 existing network (and there are no non-IMS stations in the bulletins considered here at
274 any significantly closer distances or covering any significant azimuthal gaps), Figure 4
275 indicates that the location uncertainty is well within these limits. The completed IMS,
276 as listed in the treaty text, contains in addition stations not currently operating that
277 would likely have improved the constraints on this event (in particular, the Luxor array
278 in Egypt: 26.0 °N 33.0 °E, not yet constructed, and the BGCA 3-component station in the
279 Central African Republic: 5.176 °N, 18.424 °E, installed but not currently operational).
280 Another IMS 3-component station, KOWA, in Mali, is now operational but was not at
281 the time of this earthquake (Data from IU.KOWA is openly available to the community
282 via IRIS). There are few opportunities for further reducing the uncertainty in the seismic
283 location estimates without additional, closer, stations. For example, there are no nearby
284 seismic events from which we could perform a calibrated or relative location estimate
285 (e.g. Douglas, 1967, and subsequent studies of joint epicentral determination and multiple
286 event location). The scarcity of seismic observations in the region also means that regional
287 3D seismic velocity models remain unrefined and uncalibrated.

288 4 Surface displacement from the 18 January 2017 289 Niger Earthquake using InSAR Data

290 In the case of remote continental earthquakes, with a sparsity of near-field seismological
291 data, the recently-developed global coverage of satellite radar offers an additional dataset
292 to which may help constrain earthquake locations, and complement those constraints
293 available from seismology. The limiting factor in locating an earthquake using satellite
294 geodesy is not directly the magnitude of the earthquake, but instead the amplitude of
295 the surface deformation, and whether any signal can be detected. Whilst the Ténéré
296 earthquake is lower magnitude than typically studied using InSAR (e.g., Weston et al,
297 2012; Funning and Garcia, 2019), other small-magnitude events have been detected in
298 the past (Lohman and Simons, 2005; Ritz et al, 2020), in cases where the earthquake is
299 very shallow, allowing higher-amplitude near-fault displacements to be expressed at the
300 surface. Whereas converting remote seismological observations to an source location can
301 be subject to major uncertainties on the scale of 10’s of kilometres, particularly relating
302 the velocity structure, geodetic measurements offer the direct detection of near-fault
303 displacement, in the ideal case where a fault breaks the surface, can determine the fault
304 location with pixel-scale resolution (typically 10’s of metres). Therefore, whilst InSAR
305 offers no constraint on the earthquake origin time, places no constraints on the rupture
306 evolution, and, for small-magnitude events, can only detect shallow sources (Mellors et al,
307 2004), it can offer a valuable complement to seismological observations, placing precise
308 constraints on the location of the rupture plane.

309 To supplement the available seismic data, we process interferometric synthetic aper-
310 ture radar (InSAR) images for the source region using data from the European Space
311 Agency’s Sentinel-1 satellites. We use acquisitions that span the earthquake date, and
312 construct interferograms using all potential pairs where the earthquake occurs within a
313 timespan of up to four consecutive acquisitions (Figure 5). Processing was carried out
314 using the LiCSAR system (Lazecký et al, 2020, to which readers are directed for a full
315 description of the processing approach). Each interferogram is processed using multilook-
316 ing factors of 5 in range and 20 in azimuth, with interferograms therefore having a spatial
317 resolution of $\sim 100 \times 100$ m per pixel. Data are then subject to spatial filtering using an
318 adaptive power spectrum filter. Due to the remote location, only ascending track data
319 were being routinely acquired at the time of our study earthquake, with a 12-day repeat
320 time. Coherence in the region at such short temporal baselines is good – the region is
321 unvegetated desert, and whilst migratory sand can cause problems for radar interferom-
322 etry, this does not appear to be the case around our earthquake, although we note that
323 the dune fields to the south and southwest show markedly lower coherence. In Supple-
324 mentary Material, Figure S2 shows average coherence prior to spatial filtering at 12, 24
325 and 36 day temporal baselines across the whole Sentinel-1 archive. As demonstrated by

326 Figure 5 and Figure 6, after spatial filtering, coherence at the wavelengths of interest
327 for earthquake-related processes is extremely high. Given the lack of major topographic
328 features, there is minimal topographically-correlated atmospheric noise, although all in-
329 terferograms are subject to long-wavelength noise presumed to result from a combination
330 of atmospheric variations and orbital effects (see Figures 5 and 6). One SAR acquisition
331 (20161216) features NE-SW orientated bands which are clearly unrelated to either the
332 regional tectonics or our study earthquake. Although the exact origin of these features
333 is uncertain, they are most likely to be atmospheric rolls. Some of the interferograms
334 shown in Figure 6, which do not span the earthquake, show significantly higher levels of
335 noise, which we presume to be atmospheric in origin, showing that even here, atmospheric
336 variability can strongly influence the detection of tectonic signals, although it does not
337 hinder our observations of the 2017 Ténéré earthquake.

338 All coseismic interferograms feature a small, roughly circular, displacement signal at
339 $\sim 19.6^\circ$ N, 10.6° E, highlighted by the black circle on Figure 5. This signal displays a
340 spatial pattern as expected for a small-magnitude earthquake, is at a wavelength where
341 we would expect the deformation signal from a $m_b 4.3$ to be (1 – 5 km, based on a rupture
342 length of ≤ 1 km following the established earthquake scaling relationships; Wells and
343 Coppersmith, 1994), is common to all interferograms that span the earthquake date, and
344 is not present in any interferograms that do not span the earthquake (see Figure 6 for
345 examples). We are therefore confident that this signal relates to our study earthquake,
346 despite the small amplitude of the observed signal.

347 To improve the resolution of this signal, we construct a simple linear stack of 3
348 fully independent interferograms (20161204-20170202, 20161228-20170226, and 20170109-
349 20170310 from Figure 5 – stack shown in Figure 7a). To remove long-wavelength atmo-
350 spheric effects, and to isolate signals at wavelengths likely to be related to a $m_b 4.3$ earth-
351 quake, we spatially filter the InSAR data using a 4-pole Butterworth filter, bandpassed
352 between 15000 and 500 metres (Figure 7b).

353 The resulting stack shows a clear, coherent line-of-sight displacement of up to 6 mm.
354 Only one lobe of the deformation field is clearly visible, and although there are indica-
355 tions on the filtered stack of opposite-polarity displacement lobes to the northeast and
356 southeast of the main deformation lobe, these are insufficiently clear to permit the deter-
357 mination of a focal mechanism. We visually assess that the causative fault plane most
358 likely lies to the southeast or northeast of the peak in displacement. The lack of a clear
359 four-lobe pattern of deformation argues against a pure strike-slip mechanism, and we
360 infer that the earthquake therefore involved either dip- or oblique-slip faulting.

361 The deformation pattern shows no clear discontinuities in phase, either on the stack
362 or on individual interferograms, suggesting that the rupture did not break the surface,
363 and that the top of the fault rupture patch is buried. That there is an observable signal
364 at all, however, from such a small-magnitude event, indicates that the earthquake must

365 have been shallow (≤ 5 km; see Mellors et al (2004); Dawson and Tregoning (2007)),
366 consistent with the lack of any clearly separated depth phases in the seismic data (see
367 Figure 2). In the case of this earthquake, located in the sandy Ténéré desert, we consider
368 it likely that the earthquake ruptured to the top of the consolidated bedrock, but that the
369 deformation signal is subsequently blanketed by overlying less consolidated sandstones,
370 less able to sustain coseismic rupture.

371 5 Conclusions and Discussion

372 Figure 7 shows both seismological and geodetic constraints on the location of the 2017
373 Ténéré earthquake. Of the four catalogue locations published by seismological agencies
374 only those from the CTBT and the initial ISC catalogue are consistent with the more
375 precise location information offered by the InSAR displacement pattern. The location
376 from the NEIC lies marginally too far east, but within its own uncertainty envelope of
377 the geodetic location, whilst the ISC-EHB location lies ~ 15 km to the east-southeast
378 of the geodetic location, substantially beyond its quoted uncertainty interval from the
379 geodetically-observed displacement signal (Figure 3). The EMSC location lies ~ 30 km
380 to the southeast of the detected surface deformation – the furthest of any of the catalogue
381 locations we consider.

382 Such differences between seismological and geodetic locations are commonly, and
383 widely observed for larger earthquakes (e.g. Weston et al, 2012). However, comparison
384 of geodetic and seismological location is not simple – the two approaches are measuring
385 slightly different aspects of the earthquake. Seismological locations like those applied to
386 this earthquake give a hypocentre – the point of rupture initiation. In contrast, geodetic
387 data like that used here has no capacity to constrain the earthquake initiation, or its rup-
388 ture process, in time, as the displacement seen in the interferograms is the result of the
389 complete earthquake rupture. In this case, we are unable to solve robustly for a causative
390 fault plane from the InSAR data, but even if we could, the earthquake hypocentre could
391 still lie anywhere on that rupture plane. For larger earthquakes, with rupture lengths
392 of > 5 km, this can pose additional location problems. However, for a small-magnitude
393 event like the 2017 Ténéré earthquake, where the rupture length is likely to be < 5 km,
394 this discrepancy between the seismological hypocentre and the geodetic fault rupture will
395 be small, compared to the uncertainties in seismological location.

396 Seismological locations are subject to uncertainty in the solid-Earth velocity structure
397 along the full ray path from source to receiver. In the case of the locations shown in Figure
398 3 and 4, the relative travel-time difference between all the locations shown is < 0.5 s
399 for regional arrivals and < 0.2 s for teleseismic arrivals. As demonstrated in Figure 2,
400 the majority of arrivals are emergent, and picking a precise onset is usually subject to
401 uncertainties on at least this magnitude. This is then compounded by the variation in

402 predicted travel times between different velocity models. Many location routines use a
403 standard global 1-dimensional velocity structure. Inclusion of the 3D Earth structure,
404 whilst possible (e.g. Simmons et al, 2021, and references therein), remains subject to
405 relatively large uncertainties in areas like Saharan Africa, where coverage from both
406 sources and stations is very poor. In this region, the variation in predicted travel times
407 between simple 1D and more complex 3D velocity models can add an additional 0.5s in
408 travel time uncertainty, equating to a spatial difference on the order of 10 – 20 km. In
409 contrast, locations based on geodetic data are subject to uncertainty derived only from
410 the very-near source elastic structure. For shallow earthquakes, in particular, the impact
411 that this has on geodetic earthquake location is minimal.

412 Seismological estimates for the magnitude of the Ténéré earthquake vary between m_b
413 4.2 (IDC) and m_b 4.7 (EMSC). Although without formally determining the amount of slip,
414 we are unable to use the InSAR data to quantitatively estimate a comparable geodetic
415 magnitude, we note that that surface displacement wavelength of the deformation imaged
416 using InSAR is perhaps longer than would be expected, particularly at the lower end of the
417 range of m_b estimates. As the InSAR deformation field captures all deformation between
418 the two acquisition dates, we cannot rule out the possibility that the displacement seen is
419 enhanced by some level of aseismic process. However, this would be rare for an earthquake
420 of this magnitude.

421 The consideration of both InSAR and seismological data for small magnitude earth-
422 quakes, as shown here, therefore demonstrates the potential for geodetic data to both
423 supplement, and potentially calibrate, seismological earthquake location, allowed the de-
424 termination of high-precision absolute spatial locations for small earthquakes with small
425 rupture lengths. Such characterisation has several potential applications. Firstly, such
426 high precision location constraints have the potential to contribute to the monitoring and
427 discrimination capabilities of the CTBT, particularly in remote areas, far from near-field
428 seismological instrumentation. Secondly, high-precision geodetic earthquake locations
429 can be used to calibrate regional seismological locations, which are often subject to large
430 systematic uncertainties due to biases in velocity structure and in network geometry.
431 Thirdly, in cases where accurate arrival times can be determined, precise locations allow
432 the use of small earthquakes in remote places to be used for the validation of tomographic
433 models for the solid-Earth velocity structure, supplementing sparse available equivalents
434 from controlled-source seismic signals (usually explosions: Bondár and McLaughlin, 2009).

435 Our study on the 2017 Ténéré therefore illustrates the potential for satellite radar
436 to supplement the monitoring capabilities of traditional seismological networks for earth-
437 quake location, particularly in remote areas, and particularly in areas with high coherence.
438 As the footprint of satellite missions, and the coverage of routine processing, expands,
439 the potential for InSAR to be brought in to routine earthquake monitoring will only
440 increase. Seismic detectability maps have long been employed to estimate thresholds

441 for the magnitudes of seismic disturbances which can confidently be detected and loca-
442 tion in a given region for a given monitoring network (e.g. Kväerna and Ringdal, 2013).
443 Going forwards, we would recommend developing from the theoretical work of Mellors
444 et al (2004); Dawson and Tregoning (2007), and building towards global detectability
445 maps for geodetic observation, although we recognise that these would need to build
446 in the limitations posed by the tradeoff between depth and magnitude of displacement
447 detectability, and time-variable nature of both decorrelation and non-tectonic (e.g., at-
448 mospheric) noise in satellite radar. Funning and Garcia (2019) suggested that there is a
449 magnitude completeness threshold for global earthquake detectability for crustal earth-
450 quakes between M_w 6.2 – 7.0 when using Sentinel-1 InSAR data. However, our study,
451 along with a growing number of others (e.g., Ganas et al, 2018; Dalaison et al, 2021; Liu
452 et al, 2021), shows that, whilst far from complete, in certain regions and for particularly
453 shallow earthquakes, there are often detectable signals even for earthquakes down to a
454 $M \sim 4$ which can be used to provide additional constraints on earthquake locations.

455 The 2017 Ténéré earthquake also illustrates the role that data not routinely available
456 to the academic community play in earthquake location. For both the USGS and the ISC
457 sets of arrivals used in our relocation (see Figure 4), restricting the arrivals used to only
458 Open Access data leads to a marked increase the location uncertainty. Whilst the InSAR
459 data used here, from the European Space Agency’s Sentinel-1 mission, is freely available,
460 the same is not necessarily true for all radar missions. Whilst the radar coherence in the
461 Ténéré is high, allowing up to resolve such small displacements, conducting such work
462 elsewhere, particularly in more vegetated environments, will likely benefit from the use
463 of a range of satellites with different mission parameters, particularly wavelength, and
464 may lead to a similar disparity between Open Access and restricted data that we see in
465 the seismological datasets.

466 Acknowledgements

467 TJC was supported in this work by the Royal Society under URF\R1\180088. TJC
468 was also supported through COMET, the UK Natural Environment Research Council’s
469 Centre for the Observation and Modelling of Earthquakes, Volcanoes, and Tectonics. We
470 thank Milan Lazecky for his assistance with processing the InSAR data, and Tim Wright
471 for useful discussions. We thank Manon Dalaison and one anonymous reviewer for their
472 comments, which have helped improve this manuscript.

473 All maps in this paper are created using GMT software (Wessel et al, 2019). Seismo-
474 grams in Figure 1 and 2 were plotted using Obspy (Beyreuther et al, 2010).

475 Data Availability

476 The published location estimates were obtained from the bulletin of the International
477 Seismological Center (ISC, 2021) [http://www.isc.ac.uk/cgi-bin/web-db-v4?event_](http://www.isc.ac.uk/cgi-bin/web-db-v4?event_id=619603285)
478 [id=619603285](http://www.isc.ac.uk/cgi-bin/web-db-v4?event_id=619603285) (ISC, last accessed February 2022) and from the European Mediterranean
479 Seismological Centre [https://www.emsc-csem.org/Earthquake/earthquake.php?id=](https://www.emsc-csem.org/Earthquake/earthquake.php?id=561096)
480 [561096](https://www.emsc-csem.org/Earthquake/earthquake.php?id=561096) (EMSC, last accessed February 2022). The USGS/NEIC solution with phase ar-
481 rival times are published on [https://earthquake.usgs.gov/earthquakes/eventpage/](https://earthquake.usgs.gov/earthquakes/eventpage/us10007u0v/executive)
482 [us10007u0v/executive](https://earthquake.usgs.gov/earthquakes/eventpage/us10007u0v/executive) (United States Geological Survey, last accessed February 2022).
483 The bayesloc program is obtained from [https://www-gs.llnl.gov/nuclear-threat-](https://www-gs.llnl.gov/nuclear-threat-reduction/nuclear-explosion-monitoring/bayesloc)
484 [reduction/nuclear-explosion-monitoring/bayesloc](https://www-gs.llnl.gov/nuclear-threat-reduction/nuclear-explosion-monitoring/bayesloc) (last accessed February 2022).
485 InSAR data we retrieved from <https://comet.nerc.ac.uk/comet-lics-portal/> (last
486 accessed February 2022). LiCSAR data contain modified Copernicus Sentinel data [2017]
487 analysed by the Centre for the Observation and Modelling of Earthquakes, Volcanoes
488 and Tectonics (COMET). LiCSAR uses JASMIN, the UK’s collaborative data analysis
489 environment (<http://jasmin.ac.uk>)”

490 Seismic waveform data was obtained from the following networks of the International
491 Federation of Digital Seismograph Networks (FDSN): BR, CA, CN, CQ, G, GE, GO, GR,
492 GT, HL, HP, HT, II, IS, IU, KO, KR, KZ, MN, NR, RO, TJ, US, XW. We gratefully ac-
493 knowledge the operators of all of the networks for providing open access to the data and to
494 the Incorporated Research Institutions for Seismology (IRIS, <https://www.iris.edu/hq/>)
495 and the various nodes of the European Integrated Data Archive (EIDA, [https://www.orfeus-](https://www.orfeus-eu.org/data/eida/nodes/)
496 [eu.org/data/eida/nodes/](https://www.orfeus-eu.org/data/eida/nodes/)) for providing access to this data.

497 References

498 Barker B, Clark M, Davis P, Fisk M, Hedlin M, Israelsson H, Khalturin V, Kim WY,
499 McLaughlin K, Meade C, North R, Orcutt J, Powell C, Richards PG, Stead R,
500 Stevens J, Vernon F, Murphy J, Wallace T (1998) Monitoring Nuclear Tests. *Science*
501 281(5385):1967–1968, DOI 10.1126/science.281.5385.1967, URL [http://dx.doi.org/](http://dx.doi.org/10.1126/science.281.5385.1967)
502 [10.1126/science.281.5385.1967](http://dx.doi.org/10.1126/science.281.5385.1967)

503 Benz H (2017) Building a National Seismic Monitoring Center: NEIC from 2000 to
504 the Present. *Seismological Research Letters* 88(2B):457–461, DOI 10.1785/0220170034,
505 URL <https://pubs.geoscienceworld.org/srl/article/88/2B/457-461/282939>

506 Beyreuther M, Barsch R, Krischer L, Megies T, Behr Y, Wassermann J (2010) ObsPy:
507 A Python Toolbox for Seismology. *Seismological Research Letters* 81:530–533, DOI
508 10.1785/gssrl.81.3.530

509 Blandford R (1974) An automatic event detector at the Tonto Forest Seismic Observa-

510 tory. *Geophysics* 39(5):633–643, DOI 10.1190/1.1440453, URL [http://dx.doi.org/](http://dx.doi.org/10.1190/1.1440453)
511 [10.1190/1.1440453](http://dx.doi.org/10.1190/1.1440453)

512 Bondár I, McLaughlin K (2009) A New Ground Truth Data Set For Seismic Studies.
513 *Seismological Research Letters* 80, DOI 10.1785/gssrl.80.3.465

514 Bondár I, Storchak D (2011) Improved location procedures at the International Seismolog-
515 ical Centre. *Geophysical Journal International* 186(3):1220–1244, DOI 10.1111/j.1365-
516 246x.2011.05107.x, URL <http://dx.doi.org/10.1111/j.1365-246x.2011.05107.x>

517 Bondár I, Myers SC, Engdahl ER, Bergman EA (2004) Epicentre accuracy based on
518 seismic network criteria. *Geophysical Journal International* 156(3):483–496, DOI
519 10.1111/j.1365-246x.2004.02070.x, URL [http://dx.doi.org/10.1111/j.1365-246x.](http://dx.doi.org/10.1111/j.1365-246x.2004.02070.x)
520 [2004.02070.x](http://dx.doi.org/10.1111/j.1365-246x.2004.02070.x)

521 Chun KY, Wu Y, Henderson GA (2011) Magnitude Estimation and Source Discrim-
522 ination: A Close Look at the 2006 and 2009 North Korean Underground Nuclear
523 Explosions. *Bulletin of the Seismological Society of America* 101(3):1315–1329, DOI
524 10.1785/0120100202, URL <http://dx.doi.org/10.1785/0120100202>

525 Dalaison M, Jolivet R, van Rijsingen E, Michel S (2021) The Interplay Between Seis-
526 mic and Aseismic Slip Along the Chaman Fault Illuminated by InSAR. *Journal of*
527 *Geophysical Research* 126, DOI 10.1029/2021JB021935

528 Davies D, Kelly DJ, Filson JR (1971) The VESPA process for the analysis of seismic
529 signals. *Nature* 232:8–13

530 Dawson J, Tregoning P (2007) Uncertainty analysis of earthquake source parameters
531 determined from InSAR: A simulation study. *Journal of Geophysical Research* 112,
532 DOI 10.1029/2007JB005209

533 Douglas A (1967) Joint Epicentre Determination. *Nature* 215(5096):47–48, DOI 10.1038/
534 215047a0, URL <http://dx.doi.org/10.1038/215047a0>

535 Funning G, Garcia A (2019) A systematic study of earthquake detectability using
536 Sentinel-1 Interferometric Wide-Swath data. *Geophysical Journal International* 216,
537 DOI 10.1093/gji/ggy426

538 Ganas A, Kourkoulis P, Briole P, Moshou A, Elias P, Parcharidis I (2018) Coseismic Dis-
539 placements from Moderate-Size Earthquakes Mapped by Sentinel-1 Differential Inter-
540 ferometry: The Case of February 2017 Gulpınar Earthquake Sequence (Biga Peninsula,
541 Turkey). *Remote Sensing* 10, DOI 10.3390/rs10071089

- 542 Gibbons SJ, Antonovskaya G, Asming V, Konechnaya YV, Kremenetskaya E, Kværna
543 T, Schweitzer J, Vaganova NV (2016) The 11 October 2010 Novaya Zemlya Earth-
544 quake: Implications for Velocity Models and Regional Event Location. *Bulletin of the*
545 *Seismological Society of America* 106(4):1470–1481, DOI 10.1785/0120150302, URL
546 <http://dx.doi.org/10.1785/0120150302>
- 547 Godey S, Bossu R, Guilbert J (2013) Improving the Mediterranean seismicity pic-
548 ture thanks to international collaborations. *Physics and Chemistry of the Earth,*
549 *Parts A/B/C* 63:3–11, DOI 10.1016/j.pce.2013.04.012, URL [https://linkinghub.](https://linkinghub.elsevier.com/retrieve/pii/S1474706513000387)
550 [elsevier.com/retrieve/pii/S1474706513000387](https://linkinghub.elsevier.com/retrieve/pii/S1474706513000387)
- 551 ISC (2021) International Seismological Centre on-line Bulletin. [https://doi.org/10.](https://doi.org/10.31905/D808B830)
552 [31905/D808B830](https://doi.org/10.31905/D808B830), DOI 10.31905/D808B830
- 553 ISC-EHB (2021) International Seismological Centre ISC-EHB dataset. [https://doi.](https://doi.org/10.31905/PY08W6S3)
554 [org/10.31905/PY08W6S3](https://doi.org/10.31905/PY08W6S3), DOI 10.31905/PY08W6S3
- 555 ISC-GEM (2021) International Seismological Centre ISC GEM earthquake catalog.
556 <https://doi.org/10.31905/d808b825>, DOI 10.31905/d808b825
- 557 Koch K (2013) Eight Years of Continuous Quality Assessment of the International Data
558 Centre (IDC) Reviewed Event Bulletin. *Bulletin of the Seismological Society of Amer-*
559 *ica* 103(1):296–305, DOI 10.1785/0120110350, URL [https://pubs.geoscienceworld.](https://pubs.geoscienceworld.org/bssa/article/103/1/296-305/331565)
560 [org/bssa/article/103/1/296-305/331565](https://pubs.geoscienceworld.org/bssa/article/103/1/296-305/331565)
- 561 Kværna T, Ringdal F (2013) Detection Capability of the Seismic Network of the Inter-
562 national Monitoring System for the Comprehensive Nuclear Test-Ban-Treaty. *Bulletin*
563 *of the Seismological Society of America* 103(2A):759–772, DOI 10.1785/0120120248,
564 URL <http://dx.doi.org/10.1785/0120120248>
- 565 Lazecký M, Spaans K, González P, Maghsoudi Y, Morishita Y, Albino F, Elliott J,
566 Greenall N, Hatton E, Hooper A, Juncu D, McDougall A, Walters RJ, Watsom C,
567 Weiss J, Wright T (2020) LiCSAR: an Automatic InSAR Tool for Measuring and Mon-
568 itoring Tectonic and Volcanic Activity. *Remote Sensing* 12, DOI 10.3390/rs12152430
- 569 Liu F, Elliott J, Craig T, Hooper A, Wright T (2021) Improving the Resolving Power of
570 InSAR for Earthquakes Using Time Series: A Case Study in Iran. *Geophysical Research*
571 *Letters* 48, DOI 10.1029/2021GL093043
- 572 Lohman R, Simons M (2005) Locations of selection small earthquakes in the Zagros
573 mountains. *Geochemistry, Geophysics, Geosystems* 6, DOI 10.1029/2004GC000849
- 574 Mellors RJ, Magistrale H, Earle P, Cogbill A (2004) Comparison of Four Moderate-
575 Size Earthquakes in Southern California Using Seismology and InSAR. *Bulletin of*

576 the Seismological Society of America 94(6):2004–2014, DOI 10.1785/0120020219, URL
577 <https://pubs.geoscienceworld.org/bssa/article/94/6/2004-2014/146971>

578 Myers SC, Johannesson G, Hanley W (2007) A Bayesian hierarchical method for
579 multiple-event seismic location. *Geophysical Journal International* 171(3):1049–1063,
580 DOI 10.1111/j.1365-246x.2007.03555.x, URL <http://dx.doi.org/10.1111/j.1365-246x.2007.03555.x>

582 Myers SC, Simmons NA, Johannesson G, Matzel E (2015) Improved Regional and
583 Teleseismic P-Wave Travel-Time Prediction and Event Location Using a Global
584 3D Velocity Model. *Bulletin of the Seismological Society of America* 105(3):1642–
585 1660, DOI 10.1785/0120140272, URL <https://pubs.geoscienceworld.org/bssa/article/105/3/1642-1660/332170>

587 Ritz J, Baize S, Ferry M, Larroque C, Audin L, Delouis B, Mathot E (2020) Surface
588 rupture and shallow fault reactivation during the 2019 MW 4.9 Le Teil earthquake,
589 France. *Communications Earth and Environment* 1, DOI 10.1038/s43247-020-0012-z

590 Rost S, Thomas C (2009) Improving Seismic Resolution Through Array Processing
591 Techniques. *Surveys in Geophysics* 30:271–299, URL <http://dx.doi.org/10.1007/s10712-009-9070-6>, doi:10.1007/s10712-009-9070-6

593 Simmons NA, Myers SC, Morency C, Chiang A, Knapp DR (2021) SPiRaL: a multiresolu-
594 tion global tomography model of seismic wave speeds and radial anisotropy variations in
595 the crust and mantle. *Geophysical Journal International* 227:1366–1391, DOI 10.1093/gji/ggab277, URL <https://academic.oup.com/gji/article/227/2/1366/6324570>

597 UN (1998) CTBT, Comprehensive Nuclear Test-Ban-Treaty. United Nations, Dept. for
598 Disarmament Affairs and Dept. of Public Information, New York. <https://www.ctbto.org/the-treaty/treaty-text/>

600 Wells D, Coppersmith K (1994) New Empirical Relationships among Magnitude, Rupture
601 Length, Rupture Width, Rupture Area, and Surface Displacement. *Bulletin of the*
602 *Seismological Society of America* 84:974–2001

603 Wessel P, Luis JF, Uieda L, Scharroo R, Wobbe F, Smith WHF, Tian D (2019) The
604 Generic Mapping Tools Version 6. *Geochemistry, Geophysics, Geosystems* 20(11):5556–
605 5564, DOI 10.1029/2019GC008515

606 Weston J, Ferreira A, Funning G (2012) Systematic comparisons of earthquake source
607 models determined using InSAR and seismic data. *Tectonophysics* 532-535, DOI 10.
608 1016/j.tecto.2012.02.001

Table 1: Routine catalogue locations for the 2017/01/18 Ténéré earthquake together with 95% confidence ellipses specified with (Smaj/Smin/Az) where Smaj and Smin are the lengths of the major and minor axes in km. ^fDepths were fixed *a priori* during location determination.

Catalogue	Origin time (UTC)	Lat (°)	Lon (°)	Dep (km)	(Smaj/Smin/Az)	m_b
IDC	21:48:19.39	19.5947	10.6106	0.0 ^f	(16.0/12.7/120°)	4.2
ISC	21:48:21.08	19.5847	10.6018	10.0 ^f	(10.6/7.6/125°)	4.3
NEIC	21:48:22.14	19.6049	10.6491	10.0 ^f	(16.0/12.7/120°)	4.6
ISC-EHB	21:48:21.08	19.5530	10.7380	10.0 ^f	(7.1/5.6/117°)	–
EMSC	21:48:21.80	19.48	10.75	10.0 ^f	(18.5/14.9/93°)	4.7

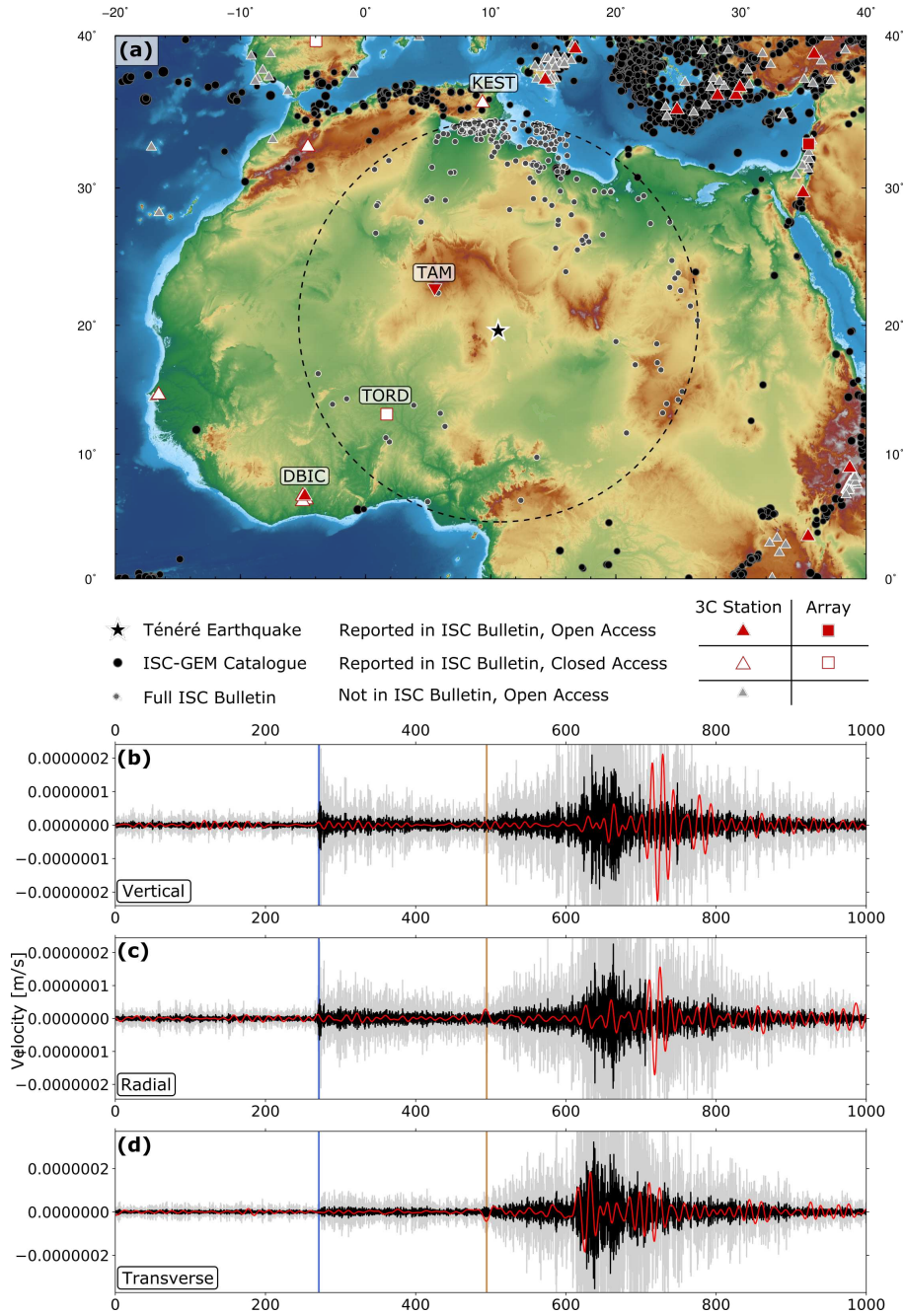


Figure 1: (a) Regional map, showing the 2017 Ténéré earthquake and distribution of observing seismometers. Red filled symbols indicate stations reported in the ISC Bulletin that are Open Access, White-filled symbols are those reported in the ISC Bulletin that are closed, grey are those Open Access 3-component stations not reported in the ISC Bulletin. Inverted red triangle shows the location of the seismometer at Tamanrasset (Algeria), usually reporting to the ISC Bulletin, but inoperative at the time of the 2017 Ténéré earthquake. Black circles show all earthquakes in the ISC-GEM catalogue. Grey circles show every earthquake recorded in the full ISC Bulletin within 15° of the 2017 Ténéré earthquake. (b) Vertical component waveform from DBIC (location shown in (a)). Black trace is filtered between 1.0 and 4.0 Hz, red between 0.02 and 0.08 Hz, to isolate surface wave arrivals, grey is the same as black, with the amplitude scaled by a factor of 5 to emphasise the body wave arrivals. Blue and green bars show the predicted P and S arrival times. (c) as in (b), but showing the radial component waveform. (d) as in (b), but showing the transverse component waveform.

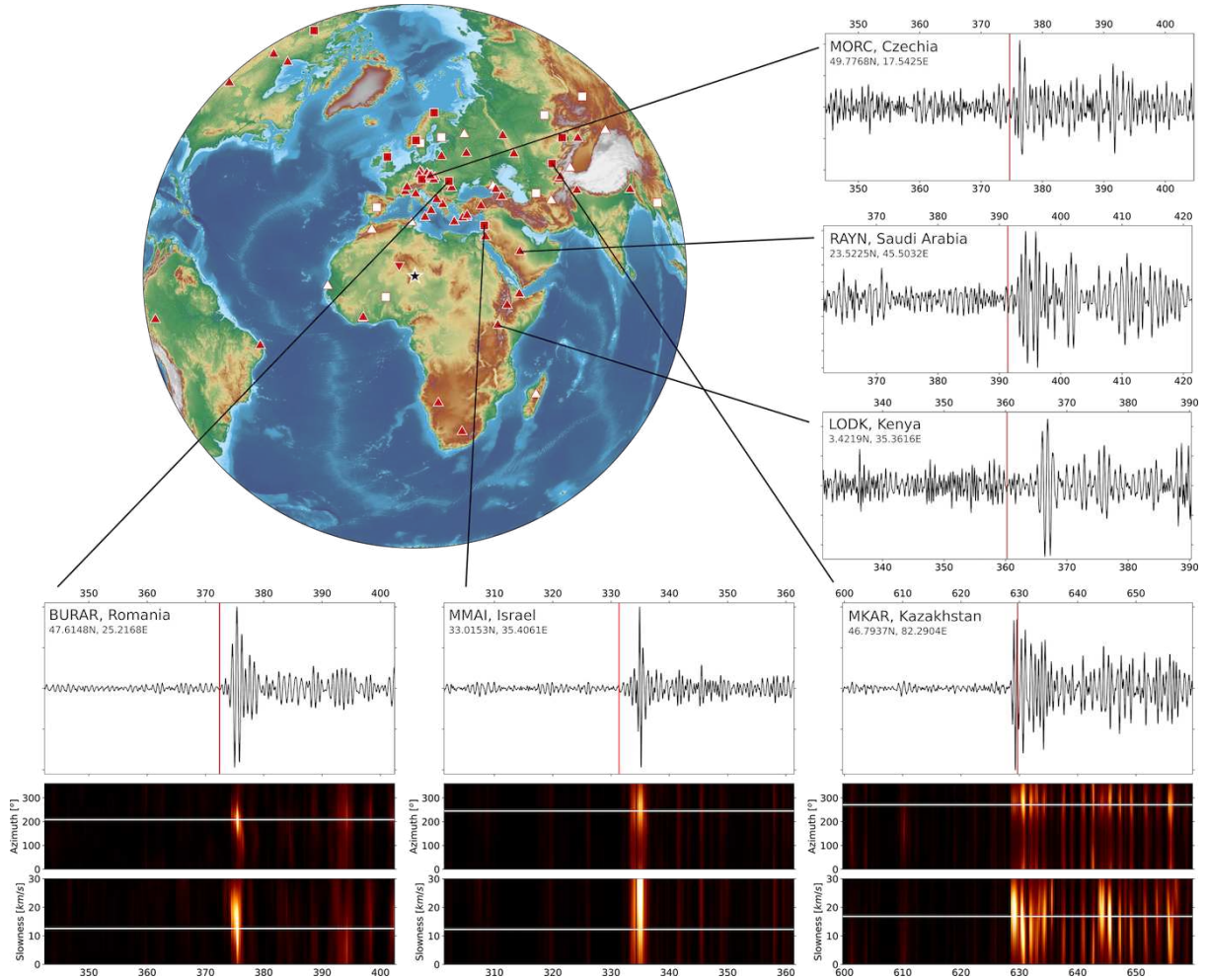


Figure 2: Global station distribution (symbols as in Figure 1). Left panels show 3 vertical component velocity waveforms, filtered between 1 – 3 Hz, from 3-component instruments RAYN, MORC, and LODK. Vertical red line shows the predicted P -wave arrival, based on the NEIC location. Lower panels show data from three small-aperture seismic arrays (Bucovina, Mount Meron, and Makanchi), again filtered between 1 – 3 Hz. Top panel shows the beamformed waveform, based on the NEIC location. Lower panels show sweeps through slowness and azimuth space (c.f. Davies et al, 1971), with colour indicating array coherence using the F -statistic (e.g. Blandford, 1974). White lines show the predicted slowness and azimuth for P -wave arrivals from the Ténéré earthquake.

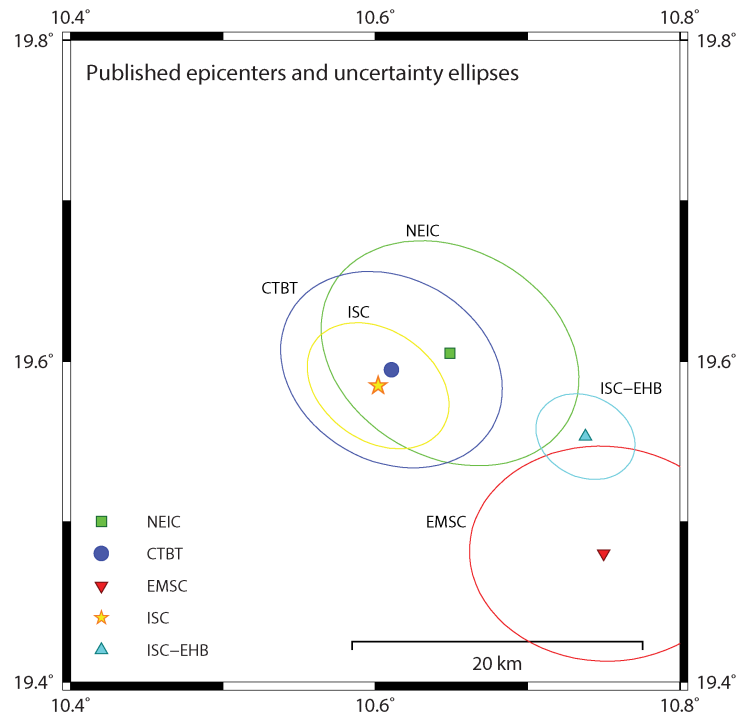


Figure 3: Published location estimates and corresponding 95% confidence ellipses for the January 18, 2017, Niger Earthquake. The epicenters are as provided in Table 1 and the 95% confidence ellipses have (S_{major}/S_{minor}/Azimuth) parameters (18.7/14.4/125°) NEIC, (16.0/12.7/120°) CTBT, (18.5/14.9/93°) EMSC, (10.6/7.6/125°) ISC, and (7.1/5.6/117°) ISC-EHB with S_{major} and S_{minor} given in km.

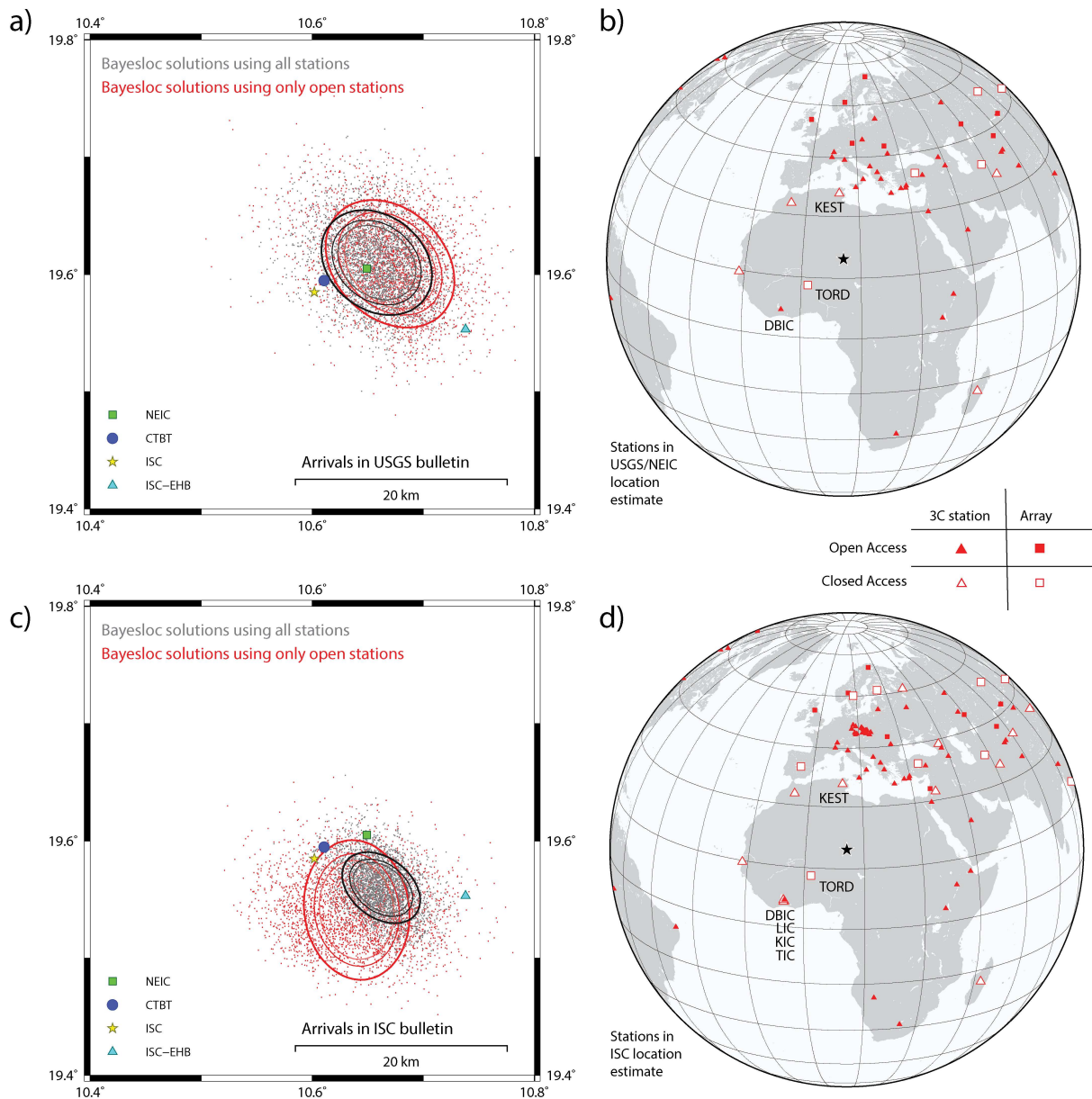


Figure 4: Location estimates obtained using the Bayesloc program with station selections as indicated. Panels (a) and (c) display clouds of the epicenters in the Bayesloc Monte Carlo Markov Chains together with the 90, 95, and 99% confidence ellipses calculated for the scatter plots. Each cloud contains 36000 points. Panels (b) and (d) display the stations used to obtain the solutions displayed in panels (a) and (c) respectively. Key stations are labelled. Stations DBIC, KIC, TIC, and LIC are within tens of kilometers of each other such that they almost appear co-located when displayed on a global scale.

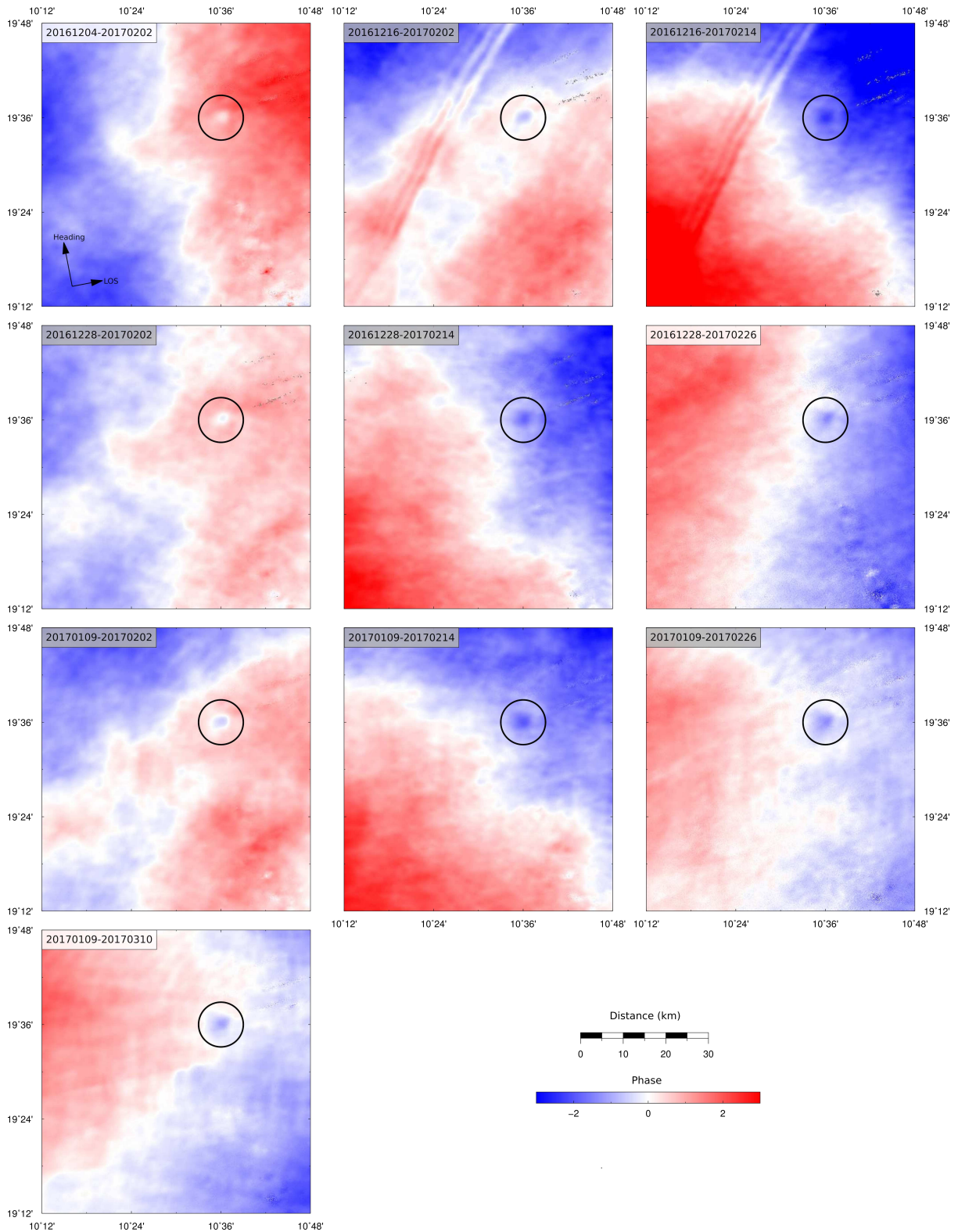


Figure 5: 10 coseismic interferograms, unwrapped. We show equivalent wrapped interferograms in Figure S1. Colour scale shows multiples of the complete phase cycle. Numeric codes in the top left of each panel indicate the SAR acquisitions used to produce each interferogram. Shading behind numeric codes indicates those independent pairs used in the stack shown in Figure 7. Black circle highlights the consistent signal identified as results from the earthquake. The final panel shows the InSAR coherence for a single interferogram.

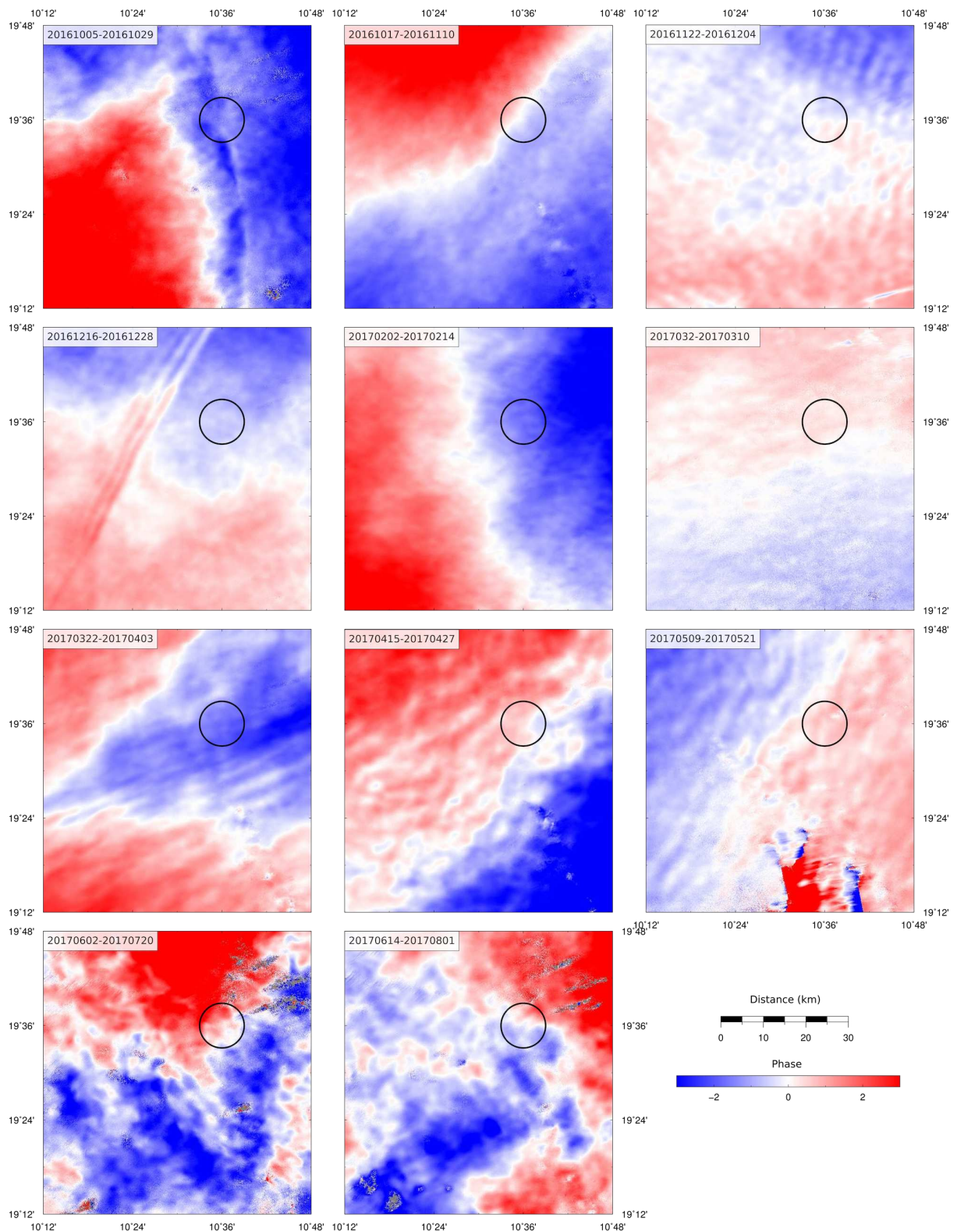


Figure 6: 11 interferograms, unwrapped, that do not span the date of the Ténéré earthquake. Numeric codes in the top left of each panel indicate the SAR acquisitions used to produce each interferogram. Black circle highlights area in which the coseismic interferograms shown in Figure 5 show a consistent deformation signal.

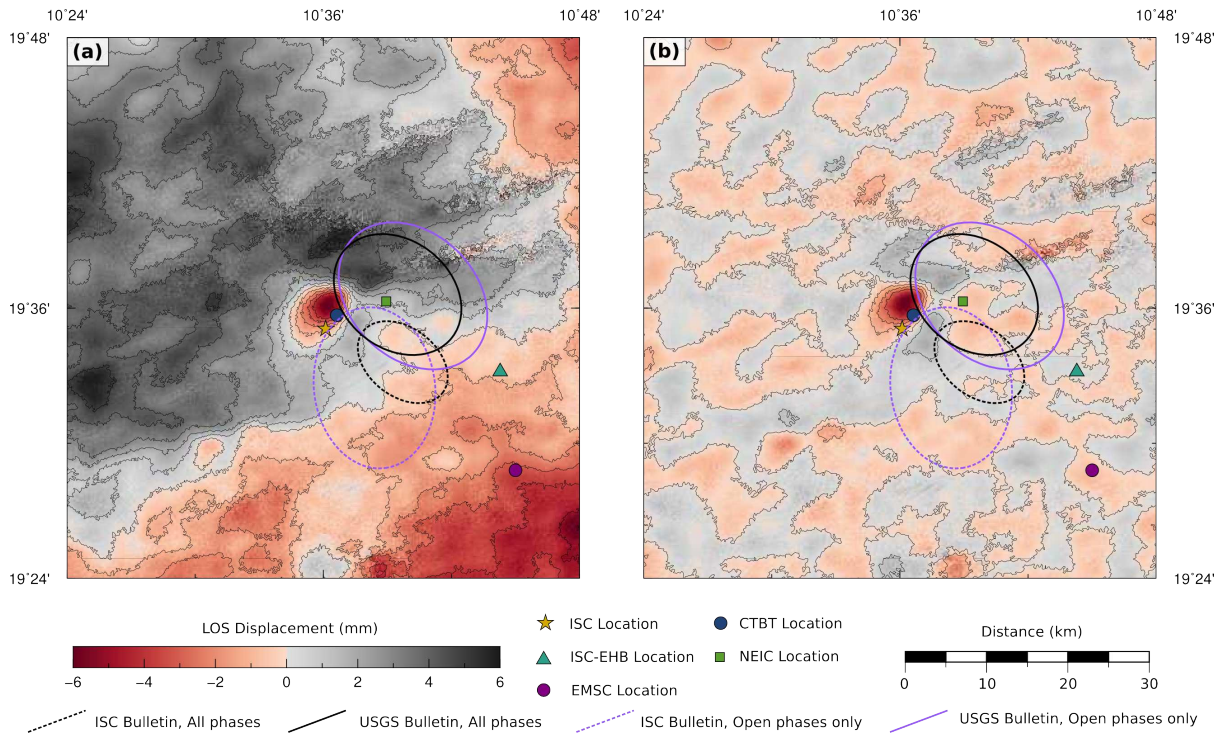


Figure 7: (a) Stacked unwrapped interferogram. (b) Stacked interferogram, filtered between 15 km and 500 m. Colour scale shows line-of-sight displacement. Symbols show seismological locations, as in Figure 3. Contours show 95% interval ellipses determined using different seismic arrival subsets, as described in Figure 4.